Rock Mechanics and Rock Engineering (2021) 54:31–46
https://doi.org/10.1007/s00603-020-02252-7

ORIGINAL PAPER

Effect of Stress Anisotropy on the Efficiency of Large-Scale Destress Blasting

Isaac Vennes[1] · Hani Mitri[1] · Damodara Reddy Chinnasane[2] · Mike Yao[2]

Received: 7 February 2020 / Accepted: 12 September 2020 / Published online: 27 September 2020

Abstract

Large-scale panel destressing is a rockburst control technique that is used to create a stress shadow in the ore pillar to be mined. The technique aims to reduce the pillar burst proneness by deviating the major induced principal stresses away from the concerned zone of interest. The destress panels, situated in the pillar hanging wall, are choke-blasted with high explosive energy density, and the blast-induced damage in the panel is accompanied by stress dissipation and stiffness reduction due to fragmentation in the panel. These two effects are traditionally modeled holistically with stiffness and stress reduction factors α and β, respectively, applied to the destressed zone. This paper focuses on the interpretation of Phase 3 destress blasting results at Copper Cliff Mine (CCM) where a stress increase (rather than decrease) was detected in the ore pillar crown, while a stress decrease was recorded in the ore pillar sill (as expected). It is hypothesized that high mining-induced stress anisotropy in the pillar crown caused blast-induced fractures to propagate in the orientation of the major principal stress, a condition that would hinder the destressing effect in that orientation. To verify the hypothesis, a series of panel anisotropic rock fragmentation and stress dissipation factors are iteratively tested in a 3-dimensional back analysis of the Phase 3 destress blast. The analysis takes into consideration the stope extraction schedule per the mine plan to better replicate the mining-induced stress condition in the panel and the ore pillar. The results show good agreement with stress measurements taken in situ using borehole stress cells installed in the ore pillar prior to destressing. The paper discusses the implications of preferential fracture propagation orientation and how it might affect the efficiency of destress blasting.

Keywords Destress blasting · Preconditioning · Rockbursts · Strainbursts · Numerical modeling

Abbreviations

CCM	Copper Cliff Mine
VRM	Vertical retreat mining
URM	Upper retreat mining
CCBM	Compact conical ended borehole monitoring
OB	Orebody
SC	Stress cell

1 Introduction

Large-scale panel destressing has been successfully implemented in Canadian hard rock mines in the mid 2000s at Fraser Mine (Andrieux 2005) and Brunswick Mine (Andrieux et al. 2003), and more recently at Copper Cliff Mine (Vennes et al. 2020). The blast pattern in all these cases was dense, with large diameter holes (> 100 mm) yielding explosive energies exceeding 200 kCal/kg. This contrasts with the more common tactical implementation of destressing for drift development and cut and fill mining (Comeau et al. 1999; O'Donnell 1992; Oliver et al. 1987), where the explosive energy per targeted mass is much lower. The aim of panel destressing is to create a stress shadow which encompasses the critical mining regions, and the geomechanical effect of panel destressing was first quantified with the back analysis of the first destressing phase at Copper Cliff Mine (CCM). A holistic modeling approach established by Tang and Mitri (2001) was implemented in a back analysis, and the

✉ Isaac Vennes
isaac.vennes@mail.mcgill.ca

[1] Department of Mining and Materials Engineering, McGill University, Montreal H3A 0E8, Canada

[2] Vale Canada Ltd, Copper Cliff P0M 1N0, Canada

phase 1 study determined a rock fragmentation factor α of 0.05 and a stress dissipation factor β of 0.95 (Vennes et al. 2020). The validation results indicate that the destress panel is highly fractured, releasing most of the panel's in situ stresses. The computed stress changes in the stress shadow zone, which are in this case the diminishing pillar stopes, confirmed the benefits of destressing. The volume of ore at risk in the stress shadow was reduced significantly. This confirms that part of the benefits of destressing is the lowered stiffness of the panel resulting in stress release.

In this paper, Tang and Mitri's holistic destressing model is modified for the Phase 3 destress blast at CCM. The immediate stress redistribution following the Phase 3 blast could not be explained with the isotropic model adopted for the Phase 1 blast, i.e., one value for α, and one value for β in all directions. The anisotropic destressing effect hypothesized by Saharan and Mitri (2009) is, therefore, explored. In his model, Saharan proposed that the degree of stress dissipation is influenced by the orientation of the in situ principal stresses, whereby the stress dissipation factor β_1 in the major principal stress direction is likely to be less than β_2 in the minor principal stress direction. The phenomenon is illustrated by Saharan and Mitri (2009) with a single-borehole, dynamic finite element model under bi-axial loading representing major and minor principal field stresses. The blast wave was simulated by a pressure pulse as a function of time. The resulting blast-induced fractures are found to be predominantly in the direction of major principal stresses. The model also showed an increase in the major principal stress magnitude along the fracture propagation direction.

Another issue that is examined in the study is the effect of slight variation of the orientation of the stress cell. The installation of stress cells in the field is tedious and prone to human errors. Variations in stress cell orientation due to possible human error are, therefore, evaluated. Bearing in mind that the stress cells used in the experimental program are uniaxial, a slight variation in orientation could lead to different stress change results.

This article is divided into 3 sections. In the first section, the Phase 3 destress at CCM is described and the measured stress changes are presented. In the second section, the stress change data are validated based on adjoining stress cell behavior. For Phase 3 blast, the behavior of stress cell SC3 installed in 9550 sill appears to be unusual showing a stress increase rather than a stress decrease in the shadow zone. This is analyzed in the third section, where the anisotropic destress model by Saharan and Mitri (2009) is applied to Phase 3 blast. The analysis shows that after accounting for possible stress cell orientation error, the anisotropic model is validated for the Phase 3 blast.

2 Copper Cliff Mine

Copper Cliff Mine is an underground hard rock metal mine located in Copper Cliff, near Sudbury, Ontario, Canada. The mine is currently operated by Vale Canada Ltd and is exploiting multiple orebodies. The orebody of interest is 100 OB, which is steeply dipping and pipe shaped, extending 1300 m vertically and around 150 m horizontally. The 100 OB is composed of massive to heavily disseminated inclusions of sulfide mineralization, with a sharp contact between the ore and host rock. The diminishing pillar in 100 OB was formed by a bottom up mining front from 3500 to 3050 L and a bottom up mining front from 4200 to 3710 L. Before any destressing, the bulk of the diminishing pillar is subjected to a major principal stress of 50–60 MPa in approximately the E–W direction (Vennes et al. 2020). At the periphery of mined and backfilled stopes, the major principal stress exceeds 100 MPa. Even higher mining-induced stress in the diminishing pillar was anticipated and a large-scale pillar-wide destressing program was implemented to facilitate the pillar recovery. The destressing program was implemented in four phases, each phase shielding a portion of the diminishing pillar. At the time of this study, 4 stopes are extracted in the diminishing pillar and 3 destress panel phases were blasted. The extraction and destressing sequence are provided in Table 1.

A numerical modeling back analysis of the Phase 1 destress blast showed that the destressing effect of the phase 1 panels was high, with a rock fragmentation factor (α) of 0.05 and a stress reduction factor (β) of 0.95 (Vennes et al. 2020). The Phase 2 destress blast between 3880 and 3710 L yielded the same stress reduction and rock fragmentation effect as the Phase 1 blast. The stress shadow created by the two destress blasts encompasses the 4 stopes that are mined up to the Phase 3 blast. The completed destress blast phases and the mined stopes at the time of this study are shown in Fig. 1.

Table 1 Mining sequence of 100 OB diminishing pillar before implementation of the Phase 3 destress blast. VRM stopes are mined in lifts bottom up from 3710 L

Stope #	Top Sill	Bottom Sill	Mining Method	Date
PHASE 1				21-Sep-15
9631	3550 L	3710 L	VRM	05-Jan-16
PHASE 2				31-Mar-16
9511	3710 L	3880 L	VRM	15-May-16
9671	N/A	3550 L	URM	20-Jun-16
9512	3710 L	3880 L	VRM	08-Oct-16
PHASE 3				06-Feb-17

URM stopes are mined with upholes from 3550 L

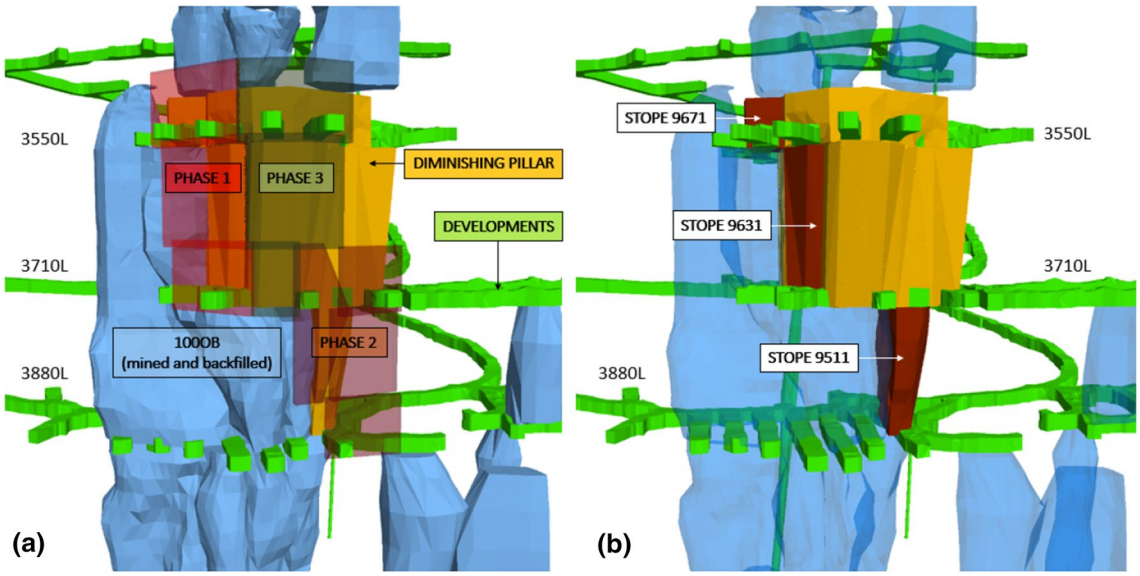

Fig. 1 Mining sequence of diminishing pillar up to Phase 3 blast. **a** Destress blasting phases, including the Phase 3 blast. **b** Mined stopes in diminishing pillar before the Phase 3 blast

2.1 Pillar Instrumentation

Ten uniaxial vibrating wire stress cells are installed in the 100 OB diminishing pillar, eight of which were installed prior the Phase 1 blast, and the other two installed prior the Phase 2 blast. The cells are oriented in either the E–W or N–S direction. The stress cells were preloaded with a wedge and platen assembly to approximately 7–8 MPa during the installation. The stress cell measurement was set as initial as soon any stress change was measured. Subsequent readings were then analyzed with reference to the initial reading to determine the changes in stress from that point onwards.

The back analysis of the Phase 3 blast, based on data from three of the stress cells, detected a significant immediate stress change after the blast. These cells are notably inside the expected stress shadow of the Phase 3 panels, and all were installed from 9550 sill. The position of the stress cells in plan view with respect to the Phase 3 panels are shown in Fig. 2.

2.2 Stress State in Pillar

Three stress cells (SC3, SC4, and SC5) logged a significant cumulative mining-induced stress increase in the pillar

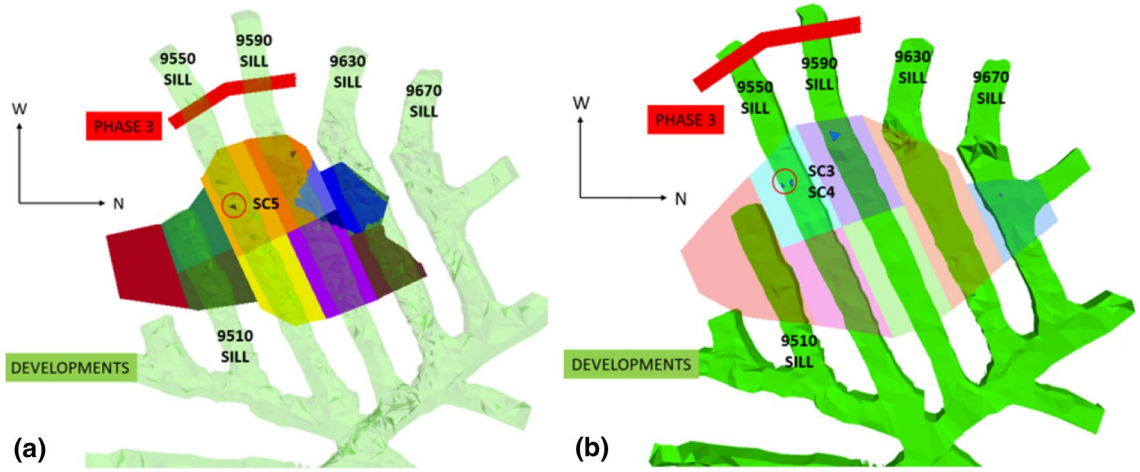

Fig. 2 Location of stress cells for validation of Phase 3 blast. **a** Uphole stress cell (SC5), installed in a 7.5 m uphole in the roof of 3550 L. **b** Downhole stress cells (SC3, SC4), installed in a 6 m vertical downhole from 3550 L

triggered by the stope 9631 crown blast. The accumulated stress change in the pillar at the time of the Phase 3 blast is, therefore, known to be high, and can be linked to high-magnitude seismic events triggered by the stope 9631 crown blast. The linear-elastic pillar-wide model constructed for this study, however, does not capture this stress accumulation. The accumulated E–W stress change and absolute major principal stress in the pillar at the time of the phase 3 blast are presented in Fig. 3. Overall, the major principal stress in the numerical model for the 9550 sill stopes ranges from 50 to 60 MPa. The computed stress accumulation in the E–W direction from the Phase 1 blast onwards ranges between 2.5 and 5.0 MPa. In contrast, Fig. 4 shows the cumulative stress change after the stope 9631 crown blast, which is an order of magnitude higher at the position of SC3, SC4, and SC5. The majority of the stress accumulation around 9550 sill can be attributed to high-magnitude seismicity ($M > 2$) which occurred after the stope 9631 crown blast. The blast triggered 7 seismic events between January and March 2016, the first two of which coincide with a rapid stress accumulation detected by SC3, SC4, and SC5.

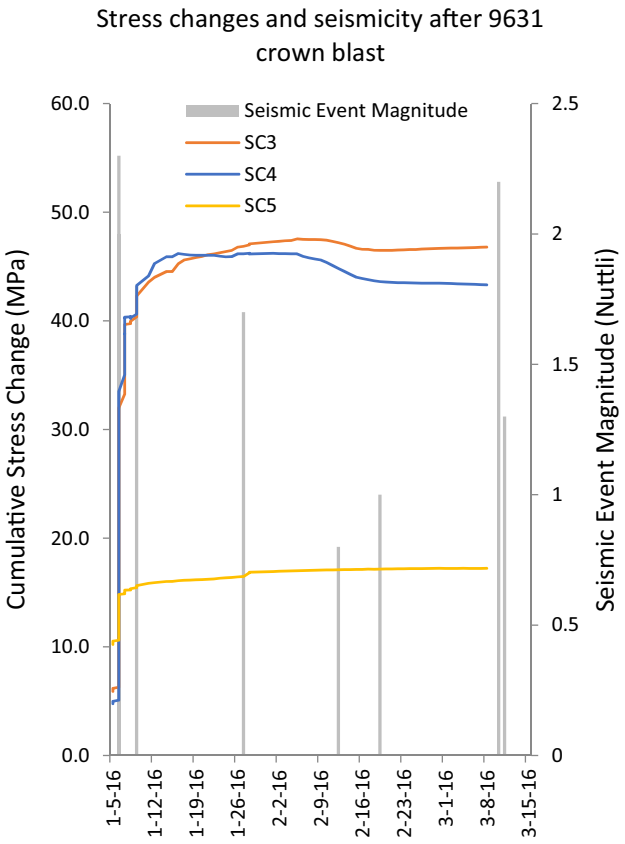

Fig. 4 cumulative stress changes measured by SC3 and SC4 overlaid with seismic event magnitudes

3 Phase 3 Blast

3.1 Blast Parameters

The Phase 3 blast is drilled from 9550 and 9590 sill on 3550 L, as well as 9590 sill on 3710 L. Two parallel

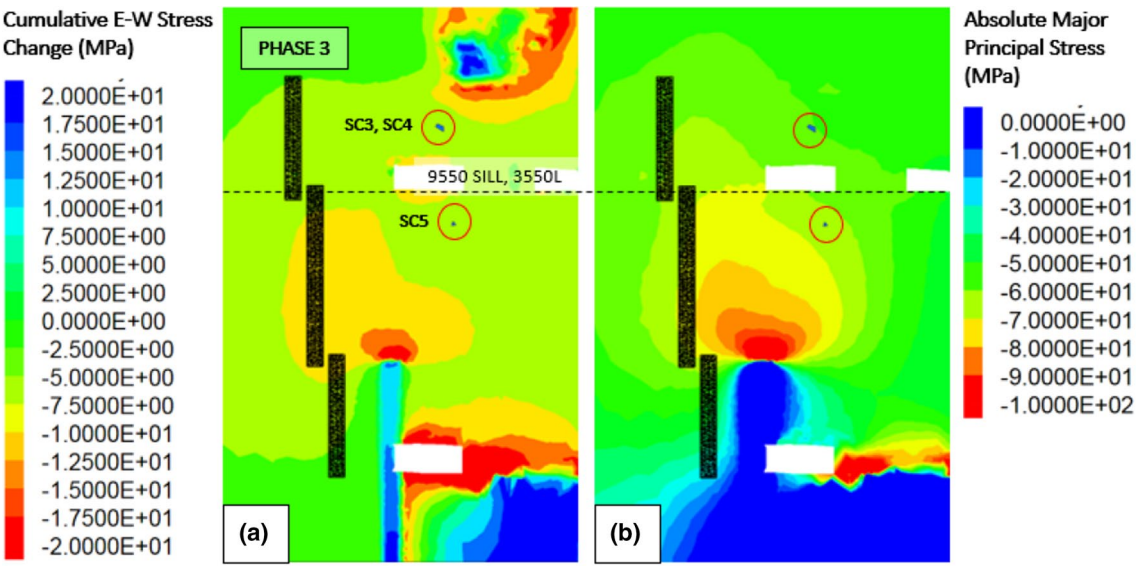

Fig. 3 E–W section view of pillar stress state in elastic model, with the positions of SC3, SC4, and SC5 highlighted. **a** Accumulated stress change between the installation of the stress cells and the Phase 3 destress blast. Stress change in the model at the position of the stress cells SC3, SC4, and SC5 range between 2.5 and 5.0 MPa. **b** Major principal stress contours before the Phase 3 destress blast. Maximum stress in the section exceeds 100 MPa at the abutment of development heading and mined stopes. Stress changes at the location of the stress cells range between 50 and 60 MPa

fanning rows of upholes and downholes, spaced 1.8 m apart, are drilled from 9550 and 9590 sill on 3550 L to form a panel approximately 36 m wide along the orebody strike and 60 m high. The upholes and downholes in each ring are staggered by 2.4 m. On the other hand, 2 rings of upholes from 3710 L, 9590 sill form a smaller 14 m wide and 18 m high panel. All holes are 114 mm in diameter, with hole lengths ranging from 5 to 36 m. The total charge is 24948 kg, with a maximum charge per delay of 306 kg and a delay of 18 ms. The toe spacing is maintained at 2.8 m by adjusting the collar length of each hole.

The immediate and cumulative stress changes for the Phase 3 blast measured by SC3, SC4, and SC5 are provided in Table 2. All other stress cells were either offline or too far to measure a significant stress change.

Tang and Mitri's holistic destressing model (2001) was first applied to the phase 3 blast with the same methodology as the phase 1 blast, as described by Vennes et al. (2020) The stress changes provided in Table 2 were used to validate the model. However, the stress increase measured by SC3 is not consistent with stress release and fragmentation model, as the numerical model cannot replicate a stress increase at the position of SC3. The discrepancy between the modeled and the measured stress changes are displayed in Fig. 5. The results from SC5 and SC4, however, are consistent with a successful blast.

Three hypotheses are tested in this study to explain the stress increase in the pillar crown. First, it is possible that the stress increase measured by SC3 local does not represent the global elastic response of the rock mass in the stress shadow of the crown panel. The stress change data, therefore, need to be validated. Second, these stress changes can be interpreted as stress wrapping into the top panel around a well-destressed sill panel. It is, therefore, possible that the stiffness of this panel is not reduced, and it is proposed that the panel rock froze in this portion of the panel. Third, stress cell orientation error is a possible cause for poor model conformity. All stress cells are uniaxial, and a slight rotation of the stress change tensor in the model can significantly change the detected stress change. The model will, therefore, be validated with an assumed orientation error of $\pm 15^{\circ}$ to establish the stress change error bounds.

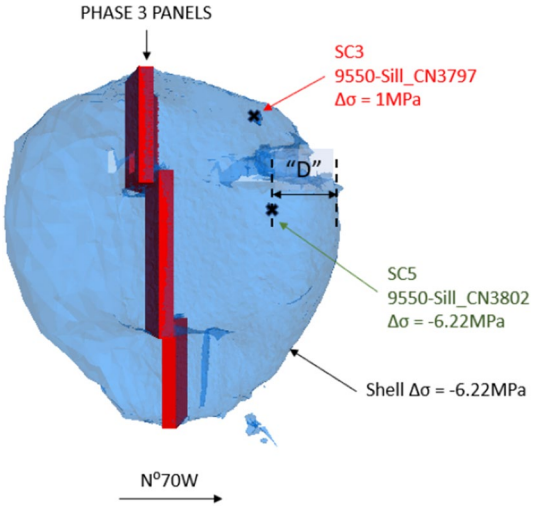

Fig. 5 Elevation view of the phase 3 panels, looking N20° E. The stress increase observed at the position of SC5 can be explained with a high destress effect, while the stress increase measured at the position of SC3 cannot. The distance "D" is measured as the smallest distance between the stress cell and the computed stress change contour with the stress change measured by the cell

3.2 Stress Cell Data Analysis

In this section, all stress cell data obtained up to and including the Phase 3 blast are analyzed to determine if the measured stress changes for phase 3 are global (at the level of the rock mass) or local (at the level or rock mass blocks). The 10 stress cells logged stress changes over the period between September 21, 2015, and February 13, 2017. Over this period, 3 destress blasts occurred (phase 1, phase 2, and phase 3). In addition, 3 stopes were extracted in the pillar, namely 9631 in the pillar sill, 9511 in the pillar sill, and 9671 in the pillar crown.

It was shown numerically by Sainoki et al. (2016) that local stress concentrations due to the heterogenous nature of a rock mass can explain the fact that rockbursts occur in rock masses where the global stress state does not attain the rock peak properties. This fact was observed by Konicek et al. (2013) in the Lazy colliery with Compact Conical ended Borehole Monitoring (CCBM) probes, were the measured in situ stresses in bursting ground were very far from the rock strength. This was also observed at CCM, where a

Table 2 Immediate and cumulative stress changes for the Phase 3 blast

SC#	Location	Orientation	Cumulative Stress Measurement (MPa)			Immediate Stress Change (MPa)
			Initial	Immediate	Stabilized	
SC3	9550 sill, uphole	E–W	51.5	57.4	52.8	5.85
SC4	9550 sill, uphole	N–S	43.9	42.1	42.1	–1 .85
SC5	9550 sill, downhole	E–W	20.4	14.1	13.1	– 6.22

survey of seismic source locations of events between March 4, 2017 and April 20, 2017 in the numerical model have a brittle shear ratio of 0.4.

It is postulated that abnormal stress changes can be attributed to this stress concentration effect. It is, therefore, important to compare the behavior of adjacent cells to establish if a stress change is global or local before attempting to validate the destress blast model. Stress change data will be also compared to the occurrence of mining and detected micro-seismicity. It is expected that adjacent or nearby stress cells will exhibit the same behavior in terms of stress change magnitude and stress change rate following a seismic event or a mining step if the stress change is global. On the other hand, isolated behavior can indicate either a measurement error or a local change in stresses.

Table 3 lists adjoining stress cells and their positions. Table 4 provides the stress stabilization rates following each mining and destressing step up to date and compares the behavior of adjoining cells. There are two occurrences where adjoining stress cell behavior does not match: after the extraction of stope 9631, between stress cells SC1 and SC2 in 9670 sill, and after Phase 3 blast, between SC3, SC4, and SC5 in 9550 sill. In the first case, SC1 measured stable stress in the N–S direction, while nearby SC2 measured a moderately fast relaxation of 0.14 MPa/day over 4 days after the crown blast. In the second case, SC4 installed in the N–S direction detected a stable stress change after the Phase 3 blast in the N–S direction, while SC3 measured a fast decay of stress of 0.77 MPa/day over 6.5 day period after the blast. SC5, installed downhole from the same drift, corroborates with neither, having measured a slow stress release of 0.28 MPa/day over 3.6 days. The cumulative stress changes over this period for SC3, SC4, and SC5 are given in Fig. 6.

SC3 is in the stress shadow of a sill panel and measured a stress increase in E–W direction. Given the E–W axis is almost normal to the panel, the stress cell data reveal that the crown panel in the Phase 3 blast did not destress stopes in its shadow, regardless of the time the stress change data are acquired. However, the sill panel successfully destressed the sill stopes, as demonstrated by SC5. Stress cell 4 also measured a stress N–S stress relaxation in the pillar crown. There are two mutually exclusive hypotheses that can explain behavior of these stress cells. First, the stress increase following the Phase 3 blast measured by SC3 is local, with a local stress relaxation that stabilizes to

Table 3 Location of adjoining stress cells

SC#	Stress Cell Name	Elevation	Orientation	Adjoining stress cells
SC1	9670-Sill_CN3800	UH (Uphole)	N–S	2 perpendicular uphole cells in 9670 sill
SC2	9670-Sill_CN3801	UH	E–W	
SC3	9550-Sill_CN3797	UH	E–W	2 perpendicular uphole cells in 9550 sill, DH cell in 9550 sill
SC4	9550-Sill_CN3798	UH	N–S	
SC5	9550-Sill_CN3802	DH (Downhole)	E–W	
SC6	9550-Sill_CN3804	Sidehole	N–S	
SC7	9590-Sill_CN3799	UH	E–W	Uphole and downhole cell in 9590 sill
SC8	9590-Sill_CN3803	DH	E–W	

Table 4 Behavior of adjoining cells following stope extraction and destress blasts

#	Phase 1	Stope 9631	Phase 2	Stope 9511	Stope 9671 L1	Stope 9671 L2	Phase 3
SC1	L–R	S	N/A	N/A	N/A	N/A	N/A
SC2	M–R	M–R	N/A	N/A	N/A	N/A	N/A
SC3	L–A	F–A	N/A	N/A	N/A	L–R	F–R
SC4	L–A	F–A	N/A	N/A	N/A	S	S
SC5	L–A	M–A	N/A	N/A	N/A	L–R	L–R
SC6	L–A	M–A	N/A	N/A	N/A	S	S
SC7	S	S	N/A	N/A	N/A	S	S
SC8	L–A	L–R	N/A	N/A	N/A	N/A	N/A

L, M, F indicate slow, moderate, and fast rate of stress change respectively. *R, S, A* indicate if stress is relaxing, stable, or accumulating. Slow stress change rates have a magnitude < 0.1 MPa/h. Fast stress change rates have a magnitude > 1.0 MPa/h

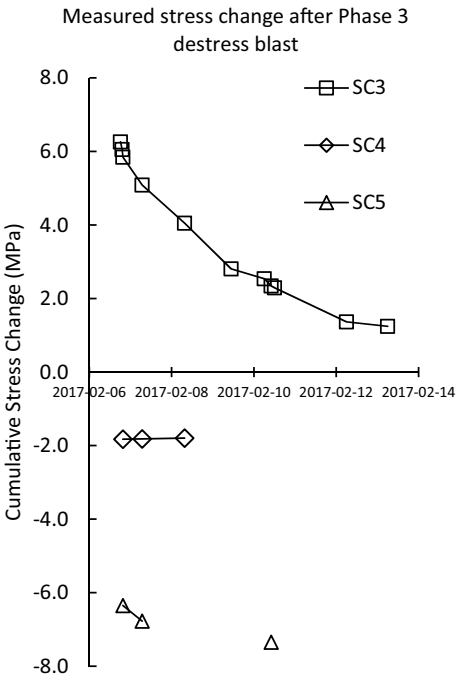

Fig. 6 Measured stress change for SC3, SC4, and SC5 after the phase 3 destress blast

global stress change. Second, the stress measured by SC4 is stable at a local level, and relaxation measured at SC3 and SC5 occurs globally.

Since the stress increase magnitude detected by SC3 is too high to replicate, the first hypothesis is deemed more likely than the second. Therefore, it is assumed that the stabilized stress at SC3 (approximately 1 MPa) is the global rock mass response to the Phase 3 blast. The phase 3 back analysis will, therefore, use this value for model validation. The corrected stress changes for the stress cells that are used to validate the phase 3 blast are given in Table 5.

3.3 Spatial Analysis of Seismic Activity

The Phase 3 destress blast was fired on 06-02-2017, at 18:15. All micro-seismic data recorded between 31-01-2017 and 12-02-1017 in the vicinity of 100 OB are analyzed to determine the effect of the Phase 3 blast on mining-induced seismicity and the efficiency of the destress blast. This timeframe was set based on the 1-week stabilizing period of the SC3 stress change measurements, as discussed in Sect. 3.2.

Overall, 319 events were recorded between 31-01-2017 and 12-02-2017, 71 of which occurred immediately after a production blast. These events are denoted as blast events and are segregated from all other recorded seismic events. The maximum position error in the data set is 25 m, with local magnitudes ranging between − 4.385 and 0.094. 72 seismic events occurred before the Phase 3 Blast, and 247 events occurred after the Phase 3 blast, including the Phase 3 blast-induced events. Figure 7 shows the cumulative seismic moment of all events recorded in the 2-week period between 3500 and 3710 L. It shows that the there is an increase in frequency and cumulative event seismic moment after the Phase 3 blast. To quantify the spatial distribution of the seismic intensity, kernel density contours for the seismic moment in the horizontal plane are computed with a 15 m diameter search circle. Figures 8 and 9 map the seismic moment kernel density contours separated between events prior and after the Phase 3 blast. The contours show that more intense seismicity occurred in the vicinity of the Phase 3 blast after it was fired. This implies the occurrence of mining-induced stress migration following the Phase 3 blast, and that the Phase 3 blast has a detectable geomechanical effect in the pillar.

The set of micro-seismic events is further classified between "crown" and "sill" events, where "crown" events are located between 3550 and 3500 L, and "sill" events are located between 3710 and 3550 L. Figures 10 shows the location of "crown" and "sill" micro-seismic events, divided between events recorded before and after the Phase 3 blast.

Table 5 Stress changes used for phase 3 validation

SC#	Orientation	Measured Stress Change (MPa)
SC3	E–W	1.00
SC4	N–S	− 1.85
SC5	E–W	− 6.22

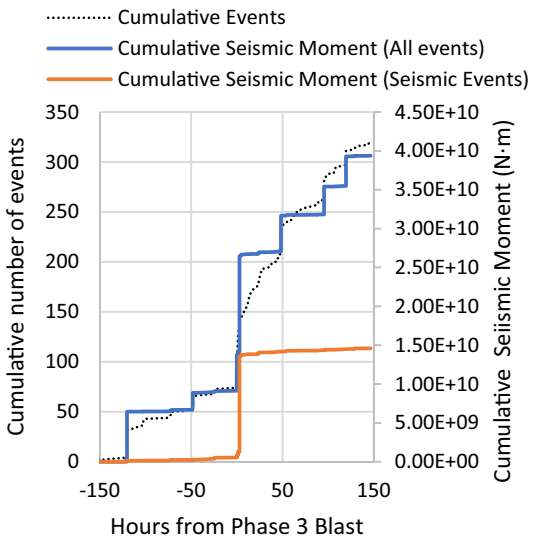

Fig. 7 Cumulative event number and seismic moment over 2-week time window. $T=0$ denotes the time of the Phase 3 blast

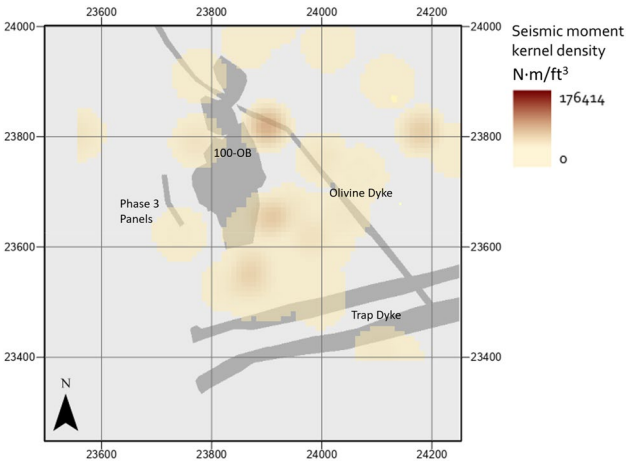

Fig. 8 Seismic moment kernel density of all events 1 week prior the Phase 3 destress blast (50′ search radius)

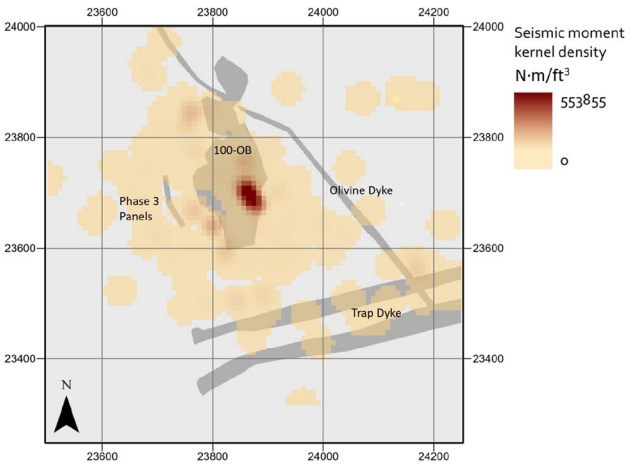

Fig. 9 Seismic moment kernel density of all events 1 week following the Phase 3 destress blast (50′ search radius)

Sphere size indicates the recorded local magnitude (M_{Local}), where $M_{\text{Local}} = -4.385$ for the smallest bubble, and -4.385, $M_{\text{Local}} = 0.094$ for the largest. In both the sill and the crown, the Phase 3 blast triggered an increase in both the magnitude and frequency of seismic activity in the vicinity of the remnant pillar. However, the spatial pattern of micro-seismicity differs between the two. In the sill, relatively little seismic activity is recorded in the expected stress shadow of the Phase 3 destress blast, suggesting that the destress blast succeeded in reducing the stress in the stress shadow stopes. Seismic activities mainly occurred in the stress window between 100 and 900 OB, to the South of the remnant pillar, with some activity to the North of the panels. Overall, the spatial distribution of seismic activity indicates stress wrapping around the panel between 3710 and 3550 L. On the other hand, crown seismicity triggered by the Phase 3 blast occurred to the North of the Phase 3 blast, around previously

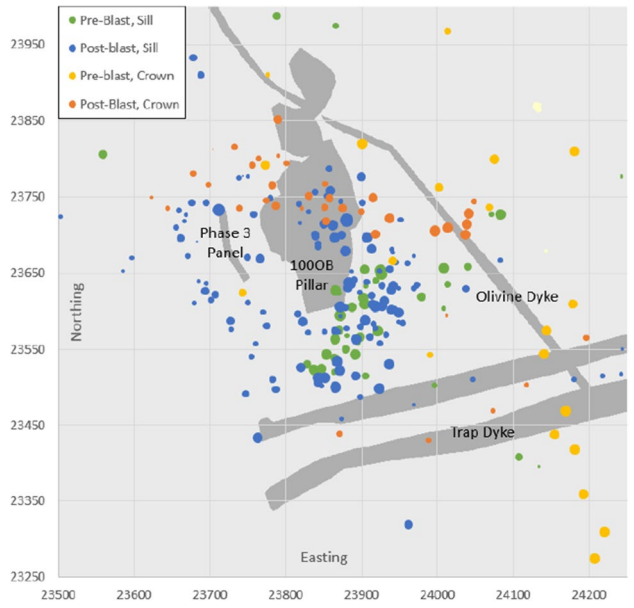

Fig. 10 Seismic events divided between sill and crown events 1 week before and after the Phase 3 blast. Sphere size denotes the local magnitude, where $M_{\text{Local}} = -4.385$ for the smallest sphere, and -4.385, $M_{\text{Local}} = 0.094$ for the largest

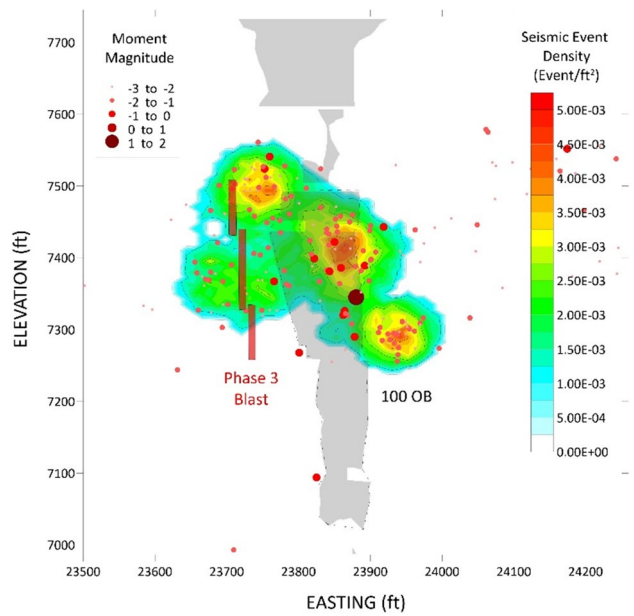

Fig. 11 Seismic event density of all seismic events after Phase 3 blast

mined stopes in the 900 OB. No seismic events are recorded to the South. This pattern suggests partial and weaker stress wrapping around the crown relative to the sill. The above trends are further supported by Fig. 11, which shows the seismic event density in section view. In the crown, the event density is higher near the panel, suggesting that little stress

migration has occurred. In the sill, high event density occurs further behind panel, indicating a greater destressing effect due to stress migrating further away from panel.

4 Methodology

4.1 Pillar Wide Model Construction

4.1.1 Model Geometry

The numerical model of the remnant pillar is constructed in Rhino and discretized in Kubrix. The numerical model is solved with the finite difference method in FLAC3D. The model geometry is shown in Fig. 12. The surfaces of unmined stopes and panels are generated from the planned stope and panel geometries, while current developments and mined stope surfaces are generated from cavity monitoring scans, i.e., they are as built. The external boundary is set outside the 1% zone of influence of the remnant pillar, with final model dimensions of 840 m in the E–W (X) direction, 800 m in the N–S (Y) direction and 700 m in the depth (Z) direction.

4.1.2 Boundary Conditions

A gravity body force is applied to the entire model. Except for the bottom face which is fixed in the z direction, all other faces are free in all directions and are subjected to boundary tractions calibrated to follow the Sudbury regional stress gradients as follows.

$$\sigma_1 = 10.82 + 0.0407 \cdot D, \tag{1}$$

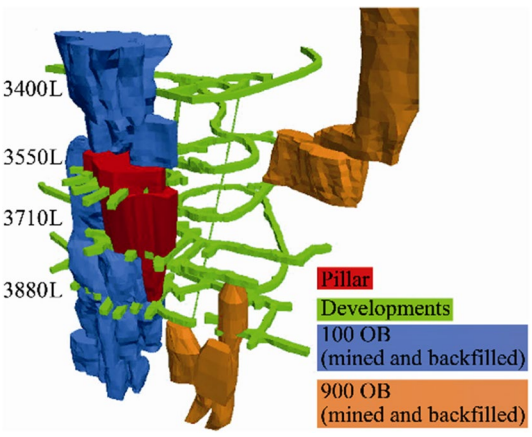

Fig. 12 3D numerical model of the remnant ore pillar in 100 OB (Vennes et al, 2020)

$$\sigma_2 = 8.68 + 0.0326 \cdot D, \tag{2}$$

$$\sigma_3 = 0.0292 \cdot D, \tag{3}$$

where D is the depth below surface in meters. The far-field minor principal stress σ_3 is assumed to be vertical, while the far-field major principal stress σ_1 is estimated to be in the N12° W direction.

4.1.3 Material Properties

All materials are linear elastic and isotropic. Their properties are provided in Table 6

4.1.4 Meshing

A mesh sensitivity analysis was conducted in a simplified pillar model to determine the required grid point spacing on the surface of the stopes and the surface of the panels. The final grid spacing for the panels and the stopes was set at 0.75 and 3 m, respectively. Model boundary grid spacing was set at 25 m, and geological domain boundary grid spacing was set at 10 m.

4.2 Anisotropic Rock Fragmentation and Stress Reduction

Previous research (Vennes et al. 2020) has shown that the stress changes in the panel stress shadow can be replicated with the rock fragmentation factor and stress reduction factor holistic model proposed by Tang and Mitri (2001). The model was applied to the Copper Cliff Mine Phase 1 destress blast panels and good conformity was obtained between the numerical model when a high stress release and rock fragmentation effect was applied to the panel. For the Phase 3 blast, the same methodology was at first adopted but could not replicate the measured stress changes. In this paper, the anisotropic destressing model proposed by Saharan and Mitri (2009) is therefore adopted for the back analysis, and it is hypothesized that the high mining-induced stress

Table 6 Model material properties

Rock specimen	Elastic properties			
	E_{intact} (GPa)	$E_{rockmass}$ (GPa)	ν	γ (kN/m^3)
Host rock	48	24.96	0.18	28.5
Orebody	52	27.6	0.19	36.3
Trap Dyke	60	60	0.22	28.5
Olivine Dyke	N/A	10	0.25	28.5
Backfill	N/A	2	0.3	20

magnitude and anisotropy in the pillar crown caused poor destressing in the crown panel.

Anisotropic stress conditions suppress the tensile stress perpendicular to the pre-blasting major principal stress axis, favoring the initiation of mode II fractures propagating in the direction of the major principal stress. Yang and Ding (2018) conducted a caustics experiment to determine the behavior of blast-induced cracks under loading. The experiment found that increasing the level of stress anisotropy decreases propagation time, increases tendency for propagation to occur in the direction of σ_1, increases severity of mode II fractures, and increases deflection angle of crack. With pre-existing crack introduced in the plate, it was found that blast-induced cracks still extend preferentially in the direction of σ_1. The same experimental setup was used to study the wave propagation in a jointed medium (Yang et al. 2016). It was found that cracks did not propagate across a pre-existing fracture. The same pattern was observed where blast-induced fractures could only propagate from the tips of the pre-existing fractures in the direction of the major principal stress.

Multiple numerical modeling studies have been conducted to investigate blasting-induced crack propagation in rocks, reporting similar behavior. Zhu et al. (2007) found partial reflection and transmission across cracks filled with unconsolidated soil as joint material, with no crack propagation across joints. The presence of air in a joint further reduces amplitude of transmitted stress waves. Ma and An (2008) varied uniaxial loading of their model up to 50 MPa, where all fractures propagated in the major principal stress direction. The effect was detectable with a deviatoric stress of just 2 MPa. These studies suggest that pre-existing fracture orientation may not be the dominant factor in the preferential orientation of blast-induced fractures, and therefore the overall destressing effect. However, it is not yet clear to what extent preferential fracture propagation will affect the stress release and rock fragmentation for a destress blast.

Considering this mechanism, Saharan and Mitri (2009) postulates with this model that the stress reduction effect is anisotropic, with a lower stress release effect in the direction of the major principal stress. The anisotropic stress release effect is expressed as:

$$\beta_{ij} = \left(\frac{\left(\sigma_{ij} \text{ before destress blasting}\right) - \left(\sigma_{ij} \text{ after destress blasting}\right)}{\sigma_{ij} \text{ before destress blasting}} \right) \times 100\%, \tag{3}$$

where β_{ij} is the stress relaxation to σ_i at measuring point on the jth Cartesian plane. σ_{ij} is the ith major principal stress at measuring point on the jth Cartesian plane. i is the principal stress identifier (1,2,3). j is the Cartesian plane identifier (x, y, z)

The effect has been quantified by Saharan and Mitri (2009) in a biaxially loaded blast damage model, where the models reported an increase in stress in the direction of the major principal stress due to fracture alignment, as well as stiffening of the rock due to the increase in stress magnitude. Stress relaxation is only achieved in the direction of the intermediate stress. The stress increase, however, is local to the blasthole and the blasting-induced fracture plane. The stiffening and stress increase effect around the borehole in the orientation of σ_1 may explain the reported stress increase in the targeted rock mass. At CCM, a stress increase was measured not in the targeted mass itself but in the expected stress shadow of the Phase 3 crown panel following the Phase 3 Blast. It is not yet clear to what extent a local stress increase around the blasthole affects the overall stress state in the panel stress shadow, and this mechanism has yet to be validated based on field measurements.

In this paper, the mechanism of preferential fracture propagation is implemented holistically, where a very low blasting-induced stress relaxation effect and stiffness reduction effect is applied in the direction of the preferential fracture propagation. The back analysis of the anisotropic model with CCM field data will shed light on the effect of the stress state prior to blasting on the success of a destress blast.

4.3 Back Analysis

In this study, a holistic destressing model is applied to the phase 3 destress panels. The pre-destress stress state is subtracted from the post-destress stress state to obtain stress change contours. Two methods were considered to measure the discrepancy between measured and modeled stress changes. The first method is simply the absolute value of the stress change difference at the position of the stress cell. However, this method is sensitive to the position of the stress cell in addition to the destress blast parameters and can provide confounding trends if the stress cell is poorly positioned. For example, if the stress cell is in a position where the stress change contours are closely spaced, i.e., showing a steep gradient, a small spatial discrepancy between the model and the field can cause large fluctuations in the stress difference at the position of the cell. Due to this limitation, the second method based on calculating the distance "D" between the stress cell position and a 3D contour surface representing perfect match (zero difference between measured and modeled stress changes) is adopted. It is found that describing the discrepancy between the numerical model and the stress cell measurements spatially with the distance "D" is a more robust approach. The distance "D" between the stress cell position and the computed stress change

contour is measured for SC3, SC4, and SC5. Low values for "*D*" indicate a good match between the model and the measured changes.

It is hypothesized that the stress increase in the crown panel stress shadow is caused by stress wrapping above the well-destressed sill panel through the poorly destressed crown panel. Poor destressing in the crown panel is simulated with an anisotropic variant of the rock fragmentation factor and stress reduction factor model proposed by Saharan and Mitri (2009). For the well-destressed sill panel, the original isotropic model is adopted. For the anisotropic model, the tendency of the hypothetical fracture plane to propagate in the direction of the major principal stress is reflected in the model by applying poor destressing factors in the orientation of σ_1.

Since the panel stress state before the Phase 3 blast is nearly transversely isotropic in the σ_2–σ_3 plane, where $\sigma_1 > > \sigma_2 \approx \sigma_3$, the σ_2 and σ_3 orientations are close to indistinguishable in the field. A second direction is therefore not imposed to the hypothetical fracture plane. Consequently, the destressing effect is the same in the direction of σ_2 and σ_3, and $\alpha_1 > \alpha_2 = \alpha_3$. A good destressing effect is applied in this plane. A damage zone of 16 times the holes diameter is assumed and treated as the targeted panel mass (Andrieux 2005), yielding a 3 m thick panel. The stress tensor applied to the destress panel zone is calculated as:

$$\left[\sigma_{123\text{destress}}\right] = \begin{bmatrix} \alpha_1\sigma_1 & 0 & 0 \\ 0 & \alpha_2\sigma_2 & 0 \\ 0 & 0 & \alpha_3\sigma_3 \end{bmatrix}, \tag{5}$$

where α_1 is the rock fragmentation factor in the direction of σ_1, α_2 is the rock fragmentation factor in the direction of σ_2, and α_3 is the rock fragmentation factor in the direction of σ_3. However, it is assumed that the fragmentation and stress release effect is transversely isotropic, with the in-plane parameters α_2 and α_3 being equal. Therefore, for all following equations, α_2 will substitute α_3. The out-of-plane rock fragmentation factor E_1 is expressed as:

$$E_1 = \alpha_1 \times E, \tag{6}$$

where E is the rock mass modulus. The out-of-plane shear modulus (G_{23}) and Poisson's ratio (ν_{23}) are calculated as:

$$\upsilon_{23} = \upsilon \times \left(2 - \alpha_1\right), \tag{7}$$

$$G_{23} = \frac{E_1}{2\left(1 + \upsilon_{23}\right)}. \tag{8}$$

The in-plane rock fragmentation factor E_2 is expressed as:

$$E_2 = E_3 = \alpha_2 \times E. \tag{9}$$

The out-of-plane Poisson ratio ν_{12} and shear modulus G_{12} are calculated based on the in-plane rock fragmentation factor:

$$\upsilon_{12} = \upsilon_{13} = \upsilon \times \left(2 - \alpha_2\right), \tag{10}$$

$$G_{12} = G_{13} = \frac{E_2}{2\left(1 + \upsilon_{12}\right)}. \tag{11}$$

The in-plane parameter α_1 is varied between 0.5 and 1, representing moderate to no destressing; while, the out-of-plane parameters α_2 is varied between 0.05 and 0.3, representing very good to good destressing. The stress reduction factor β is calculated from the applied rock fragmentation factor α assuming the relation $\alpha = 1 - \beta$. The cut-off between the well-destressed sill panel and poorly destress crown panel is set as either the floor or the roof of 3550 L.

In addition, the elastic model at the stage of the Phase 3 blast did not capture the stress accumulation in the pillar crown associated with high micro-seismicity after the 9631 crown blast. In the first scenario ("FF"), the model far-field stresses are calibrated to obtain a stress increase tensor at the position of SC3 that matches the stress change measurements of SC3 and SC4 (51.5 MPa in the E–W direction, and 42.1 MPa in the N–S direction). In the second scenario ("FF2"), the model far-field stresses are calibrated to yield a 20.5 MPa stress increase at the location of SC5. Finally, the effect of stress cell orientation error on model conformity is investigated by rotating the stress change tensor by – 15° and + 15°. Overall, 48 models are tested, with parameters summarized in Table 7.

5 Results

The values for "*D*" obtained by comparing the model stress change contour to the stress cell data are analyzed in parametric study, where measured values for "*D*" from all models are plot with respect to the in-plane rock fragmentation factor (α_2) (see Figs. 13, 14, 15, 16 and 17). The data are then further divided based a second parameter to determine the effect of its variation on model conformity.

5.1 Analysis of Stress Cell Results in Pillar Crown (SC3 and SC4)

In Fig. 13, values of "*D*" for SC3 are plotted with respect to the in-plane input rock fragmentation factor, and then divided based on the assumed stress cell orientation error ($e = 0$ or $e = -15°$). This arrangement shows that there is very little overlap between the results for "*D*" at SC3 when no orientation error is assumed compared to values for "*D*" when a − 15° degree error is assumed. For each value of α_2, almost all measurements of "*D*" with an error of − 15° are lower than the measurement of "*D*" obtained with no orientation error. The same behavior is observed with the data from

Table 7 Phase 3 validation models

Model #	Stress State	Upper extent	α_1	β_1	α_2	β_2	Model description
1			0.05	0.95	0.05	0.95	Isotropic constitutive model applied to all panels
2			0.1	0.9	0.1	0.9	
3			0.2	0.8	0.2	0.8	
4			0.3	0.7	0.3	0.7	
5			0.5	0.5	0.05	0.95	Anisotropic constitutive model applied to all panels
6					0.1	0.9	
7					0.2	0.8	
8					0.3	0.7	
9			1	0	0.05	0.95	
10					0.1	0.9	
11					0.2	0.8	
12					0.3	0.7	
13		3550 L	1	0	1	0	Extreme case models with full extraction of sill panel, extreme variation of crown panel anisotropic parameters
14					0.05	0.95	
15			0.5	0.5	0.05	0.95	Anisotropic constitutive model applied to crown panel above 3550 L
16					0.1	0.9	
17					0.2	0.8	
18					0.3	0.7	
19			1	0	0.05	0.95	
20					0.1	0.9	
21					0.2	0.8	
22					0.3	0.7	
23		3540 L	1	0	1	0	Extreme case models with full extraction of sill panel, extreme variation of crown panel anisotropic parameters
24					0.05	0.95	
25		3540 L	0.5	0.5	0.05	0.95	Anisotropic constitutive model applied to crown panel above 3540 L
26					0.1	0.9	
27					0.2	0.8	
28					0.3	0.7	
29			1	0	0.05	0.95	
30					0.1	0.9	
31					0.2	0.8	
32					0.3	0.7	
33	FF	3540 L	0.5	0.5	0.05	0.95	Anisotropic constitutive model applied to crown panel above 3540 L. Far-field stress calibrated to match SC3 and SC4 cumulative stress increase
34					0.1	0.9	
35					0.2	0.8	
36					0.3	0.7	
37			1	0	0.05	0.95	
38					0.1	0.9	
39					0.2	0.8	
40					0.3	0.7	
41	FF2	3540 L	0.5	0.5	0.05	0.95	Anisotropic constitutive model applied to crown panel above 3540 L. Far-field stress calibrated to match SC5 cumulative stress increase
42					0.1	0.9	
43					0.2	0.8	
44					0.3	0.7	
45			1	0	0.05	0.95	
46					0.1	0.9	
47					0.2	0.8	
48					0.3	0.7	

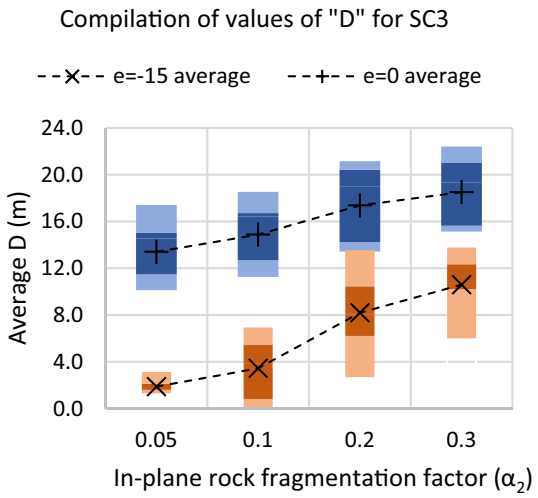

Fig. 13 Compilation of model conformity for SC3 in relation to the in-plane input parameters (α_2). Bars in red show the spread of results for "D" obtained with an error "*e*" of − 15°. The dark red shows the spread of the middle 50% of the models. Bars in blue show the spread of results for "D" with no orientation error. The dark blue shows the middle 50% of values for "D"

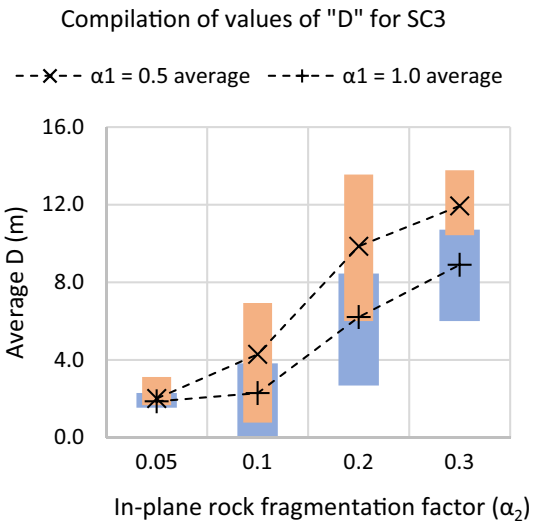

Fig. 15 Compilation of model conformity for SC3 with respect to in-plane input parameters (α_2). Bars in red show the spread of results for "D" obtained with $\alpha_1 = 0.5$. Bars in blue show the spread of results for "D" with $\alpha_1 = 1.0$

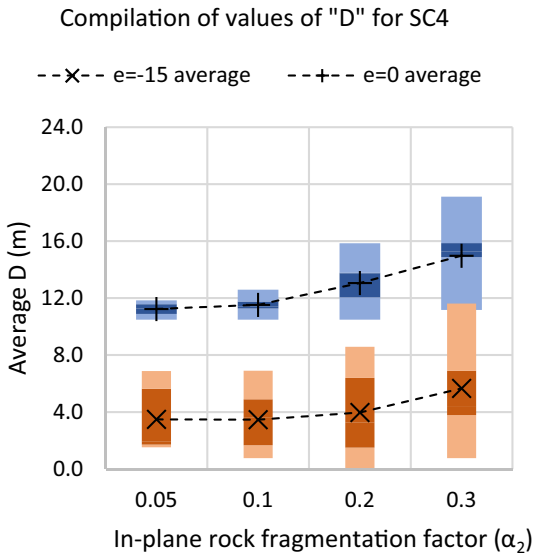

Fig. 14 Compilation of model conformity for SC4 with respect to in-plane input parameters (α_2). Bars in red show the spread of results for "D" obtained with an error "*e*" of − 15°. The dark red shows the spread of the middle 50% of the models. Bars in blue show the spread of results for "D" with no orientation error. The dark blue shows the middle 50% of values for "D"

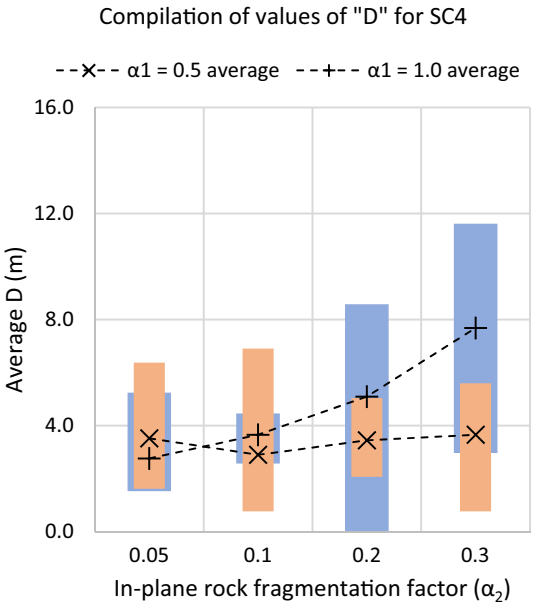

Fig. 16 Compilation of model conformity for SC4 with respect to in-plane input parameters (α_2). Bars in red show the spread of results for "D" obtained with $\alpha_1 = 1.0$. Bars in blue show the spread of results for "D" with $\alpha_1 = 0.5$. There is good overlap between the bars for $\alpha_2 = 0.05$. For higher values of α_2, models where $\alpha_1 = 0.5$ give slightly better results

SC4 (see Fig. 14), supporting the hypothesis that both cells are installed 15° counter-clockwise from the E–W axis. The split distribution of results also demonstrates how sensitive the stress cell measurement is to the installation angle of the cell, especially for the purpose of model calibration. In addition, SC3 and SC4 corroborate that a low in-plane rock fragmentation factors ($\alpha_2 = 0.05$, 0.1) yield the lowest "*D*" values overall, as shown in Figs. 13 and 14.

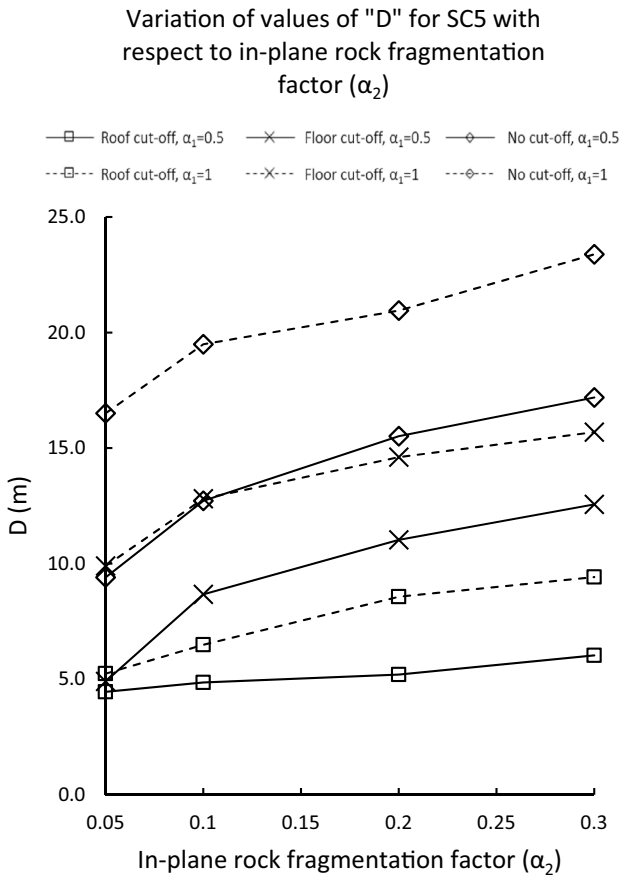

Fig. 17 Model conformity for SC5 with respect to in-plane input parameters (α_2)

Figures 15 and 16 plot the values for "*D*" obtained using a stress cell orientation error of − 15° for SC3 and SC4. The results are divided based on the out-of-plane rock fragmentation factor (α_1). There is significant overlap between each set, such that the model validation cannot discriminate between models where $\alpha_1 = 1.0$ and $\alpha_1 = 0.5$ assuming low values of α_2. The input parameter $\alpha_1 = 0.5$ is retained as it is more realistic than $\alpha_1 = 1.0$.

5.2 Analysis of stress Cell Results in Pillar Sill (SC5)

For SC5, a possible cell orientation error does not need to be considered to obtain a good match between the model and stress cell results. Figure 17 compares plots the values for "*D*" with respect to the in-plane rock fragmentation factor applied to the crown panel. The results indicate a high destressing effect in the sill panels provides good model conformity, with a rock fragmentation factor and stress reduction factor of 0.05 and 0.95 in the sill panel. The results also demonstrate the sill panel stress shadow is affected by the crown panel destressing parameters. An in-plane fragmentation factor of 0.05 and an out-of-plane fragmentation factor of 0.5 in the crown panel provides the lowest values of "*D*" for SC5, in accordance with the analysis of SC3 and SC4. Figure 17 also shows that the cut-off elevation between the isotropic sill panel and the anisotropic crown panel which yields the best results is at the roof of 3550 L.

5.3 Far Field Stress

The validation of model 25–48 shows that calibrating the far-field stresses to the measured cumulative stress at SC3 and SC5 proportionally increases the stress drop in the stress shadow, providing better conformity overall. However, it is not proven that the high stress accumulation detected by SC3, SC4, and SC5 is global or local, but the validation results suggest at least a portion of the cumulative stress accumulation is global.

5.4 Stress Wrapping Effect

An extreme stress wrapping effect was simulated with models 13, 14, 23, and 24. The sill panel was modeled as a void, and the crown panel was either left intact or given an α_1 value of 1. The results for "*D*" are given in Table 8. The models showed better results with good conformity assuming no stress cell orientation error. However, the significance of the input parameters does not match field observations, namely that the crown panel is still somewhat destressed. Also, poor conformity is obtained with respect to SC5. Therefore, the stress wrapping effect alone cannot explain

Table 8 Results for models 13, 14, 23, 24, compared to model 25

Model #	Model Parameters				*D* (m)		
	Cut-off	Sill α	Crown α_1	Crown α_2	SC3	SC4	SC5
13	3450 L	null	1	1	3.8	9.5	9.3
14			1	0.05	6.5	10.2	9.0
23	3440 L	null	1	1	1.3	10.8	6.8
24			1	0.05	4.4	10.8	8.2
25	3440 L	0.05	0.5	0.05	15.1	10.7	4.2

Stress cell orientation error $e = 0$.

Table 9 Conformity results for model 25

SC#	D (m)		
	$e=-15$	$e=0$	$e=15$
SC3	1.7	15.1	3.1
SC4	1.8	10.7	0.9
SC5	7.8	4.2	13.5

the stress increase in the sill, and the examination of the stress change contours for the crown panel showed that the combination of stress wrapping around crown pillar and stress cell orientation error is the most likely explanation for the measured stress increase.

5.5 Conclusion of Parametric Study

The results from SC3 and SC4 support a low out-of-plane destressing effect ($\alpha_1 = 0.5$) and a high in-plane destressing effect ($\alpha_2 = 0.05$) for the crown panel. However, an orientation error for both SC3 and SC4 of − 15° needs to be considered to obtain an excellent correlation between the model and the stress cell measurements. The stress increase detected by SC3 is therefore caused by a combination of stress wrapping around the sill panel through a weakly destressed crown panel and stress wrapping around the weakly destressed crown panel. For the sill panel, a good match was obtained for SC5 with a high and uniform destressing effect in all direction ($\alpha = 0.05$). The best elevation cut-off between the isotropic sill panel and anisotropic crown panel is found to be at the roof of 3550 L. Calibrating the far-field stresses to match the cumulative stress change measurements for SC3, SC4, and SC5 yields better conformity, but the portion of the stress increase which is due to a global pillar response is unknown. Based on these conclusions, model 25 is deemed to be the most likely representation of the phase 3 blast. The values for "*D*" are shown in Table 9 with respect to the stress cell and the error "*e*".

5.6 Comparison with Field Observations

Rock displacement into the destress blast cross cuts was observed following the phase 3 blast, with good rock displacement in 9550 sill on 3550 L, and poor displacement in 9550 sill on 3710 L. These observations suggest that the blast choked around 3710 L, causing poor destressing in the vicinity of 3710 L. These observations can conform with the results of the numerical modeling discussed in the previous section, but no conclusive analysis of the quality of destressing around 3710 L can be done with the numerical model with the available stress change data. The stress cells SC3, SC4, and SC5 are all installed from 3550 L, and only provide significant stress changes for the quality of destressing at the elevation of 3550 L. SC9 and SC10 are both installed from 3710 L but are too far from the phase 3 panels to discriminate between a poor destress blast and a good destress blast. For 3550 L, the back analysis concluded that poor destressing occurred in roof and good destressing in the floor, and it is postulated that the displacement which was observed on 3550 L stems from the well-destressed portion of the phase 3 blast in the floor.

6 Conclusions

The destress blasting program at Copper Cliff Mine has consistently produced stress reduction in the ore pillar and this was successfully modeled with high rock fragmentation and stress reduction factors in the destress-blasted panel. The phase 3 blast on the other hand unexpectedly resulted in stress increase in the crown panel in the stress shadow zone. This increase could not be replicated in the numerical model with the holistic stress reduction and rock fragmentation approach using isotropic α and β values in all directions. In this paper, it is postulated that the high mining-induced stress has caused the destress panel to fracture unevenly when blasted. The anisotropic destressing model originally hypothesized by Saharan and Mitri (2009) was, therefore, adopted for the crown panel. With this model, Saharan proposed that the degree of stiffness reduction and stress dissipation is influenced by the orientation of the mining-induced principal stresses prior to blasting. With this, it has been possible to explain the reason for the observed stress increase in the crown panel stress shadow zone. It was finally determined that crown panel fragmentation factor in the direction of σ_1 is as high as $\alpha_1 = 0.5$ suggesting poor fragmentation, while in the directions of σ_2 and σ_3, $\alpha_2 = 0.05$, suggesting strong fragmentation. Another issue that is discussed is the effect of slight variation of the orientation of the stress cell. Overall, it is shown that a stress cell orientation variation of 15° due to possible human error during installation could lead to a variation of the distance between the stress cell and the modeled stress change contour of up to 10 m. Hence, this must be taken into consideration when explaining the measured stress in the crown. Overall, the anisotropic stress release and fragmentation effect due to preferential fracture propagation was quantified, where the stress release and fragmentation effect normal to σ_1 is at least double the effect in the orientation of σ_1.

Acknowledgements This work is financially supported by a joint grant from MITACS Canada and Vale Canada Ltd (Project IT07425), and the MEDA fellowship program of the McGill faculty of Engineering. The authors are grateful for their support. Technical and operational input

along with the collaboration in developing these destress programs at Vale's Copper Cliff Mine are greatly appreciated.

Funding This work is financially supported by a joint grant from MITACS Canada and Vale Canada Ltd (Project IT07425), and the MEDA fellowship program of the McGill faculty of Engineering.

Compliance with Ethical Standards

Conflict of interest The authors declare that they have no conflict of interest.

References

Andrieux P (2005) Application of rock engineering systems to large-scale confined destress blasts in underground pillars. Laval University, Quebec

Andrieux P, Brummer R, Mortazavi A, Liu Q, Simser BP (2003) Large-Scale panel destress blast at Brunswick Mine CIM bulletin:78–87

Comeau W, Mitri HS, Mohammed MM, Tang B (1999) World-wide survey of destress blasting practice in deep hard rock mines. In: Paper presented at the 25th Annual Conference on Explosives and Blasting Technique

Konicek P, Soucek K, Stas L, Singh R (2013) Long-hole destress blasting for rockburst control during deep underground mining. Int J Rock Mech Min Sci. https://doi.org/10.1016/j.ijrmms.2013.02.001

Ma GW, An XM (2008) Numerical simulation of blasting-induced rock fractures. Int J Rock Mech Min Sci 45:966–975. https://doi.org/10.1016/j.ijrmms.2007.12.002

O'Donnell JDP (1992) The use of destress blasting at Inco's Creighton Mine. In: Paper presented at the MASSMIN 92, Johannesburg

Oliver P, Wiles T, MacDonald P, O'Donnel D (1987) Rockburst control measures at Inco's Creighton Mine. In: Paper presented at the 6th Conference on Ground Control in Mining, West Virginia

Saharan MR, Mitri HS (2009) Simulations for rock fracturing by destress blasting, as applied to hard rock mining conditions. VDM Verlag, Saarbrucken

Sainoki A, Mitri HS, Yao M, Chinnasane D (2016) Discontinuum modelling approach for stress analysis at a seismic source: case study. Rock Mech Rock Eng 49:4749–4765. https://doi.org/10.1007/s00603-016-1089-7

Tang B, Mitri HS (2001) Numerical modelling of rock preconditioning by destress blasting. Ground Improv 5:1–11

Vennes I, Mitri H, Chinnasane D, Yao M (2020) Large-scale destress blasting for seismicity control in hard rock mines: a case study. Int J Min Sci Technol. https://doi.org/10.1016/j.ijmst.2020.01.005 **(in press)**

Yang R, Wang Y, Ding C (2016) Laboratory study of wave propagation due to explosion in a jointed medium. Int J Rock Mech Min Sci 81:70–78. https://doi.org/10.1016/j.ijrmms.2015.10.014

Yang LY, Ding CX (2018) Fracture mechanism due to blast-imposed loading under high static stress conditions. Int J Rock Mech Min Sci 107:150–158. https://doi.org/10.1016/j.ijrmms.2018.04.039

Zhu Z, Mohanty B, Xie H (2007) Numerical investigation of blasting-induced crack initiation and propagation in rocks. Int J Rock Mech Min Sci 44:412–424. https://doi.org/10.1016/j.ijrmms.2006.09.002